

Do Stellar Winds Prevent the Formation of Supermassive Stars by Accretion?

Daisuke Nakauchi^{1*}, Takashi Hosokawa^{2,3,4}, Kazuyuki Omukai^{1,4},
Hideyuki Saio¹ and Ken'ichi Nomoto^{5†}

¹*Astronomical Institute, Tohoku University, Aoba, Sendai 980-8578, Japan*

²*Department of Physics, Kyoto University, Oiwake-cho, Kitashirakawa, Sakyo, Kyoto 606-8502, Japan*

³*Department of Physics, The University of Tokyo, Bunkyo, Tokyo 113-0033, Japan*

⁴*Kavli Institute for Theoretical Physics, Kohn Hall, University of California, Santa Barbara, CA 93106, USA*

⁵*Kavli Institute for the Physics and Mathematics of the Universe (WPI), The University of Tokyo, Kashiwa, Chiba 277-8583, Japan*

Accepted XXX. Received YYY; in original form ZZZ

ABSTRACT

Supermassive stars (SMS; $\sim 10^5 M_{\odot}$) formed from metal-free gas in the early Universe attract attention as progenitors of supermassive black holes observed at high redshifts. To form SMSs by accretion, central protostars must accrete at as high rates as $\sim 0.1\text{--}1 M_{\odot} \text{ yr}^{-1}$. Such protostars have very extended structures with bloated envelopes, like super-giant stars, and are called super-giant protostars (SGPSs). Under the assumption of hydrostatic equilibrium, SGPSs have density inverted layers, where the luminosity becomes locally super-Eddington, near the surface. If the envelope matter is allowed to flow out, however, a stellar wind could be launched and hinder the accretion growth of SGPSs before reaching the supermassive regime. We examine whether radiation-driven winds are launched from SGPSs by constructing steady and spherically symmetric wind solutions. We find that the wind velocity does not reach the escape velocity in any case considered. This is because once the temperature falls below $\sim 10^4$ K, the opacity plummet drastically owing to the recombination of hydrogen and the acceleration ceases suddenly. This indicates that, in realistic non-steady cases, even if outflows are launched from the surface of SGPSs, they would fall back again. Such a “wind” does not result in net mass loss and does not prevent the growth of SGPSs. In conclusion, SGPSs will grow to SMSs and eventually collapse to massive BHs of $\sim 10^5 M_{\odot}$, as long as the rapid accretion is maintained.

Key words: stars: formation - stars: Population III - dark ages, reionization, first stars - early Universe.

1 INTRODUCTION

In the last decade, a number of luminous quasars (QSOs) have been discovered at redshifts greater than 6 (Fan 2006; Mortlock et al. 2011; Venemans et al. 2013; Wu et al. 2015), including the current record holder ULAS J1120+0641 at $z = 7.1$ (Mortlock et al. 2011). This means that supermassive black holes (SMBHs) of $\sim 10^9\text{--}10^{10} M_{\odot}$ have already existed in less than a billion year after the Big Bang. Such early formation poses a challenge to theories of the SMBH formation (e.g., Volonteri 2010; Haiman 2013).

Although the first stars are considered theoretically to be typically massive with $\sim 100 M_{\odot}$, and even can be

as massive as $\sim 1000 M_{\odot}$ in some circumstances, (e.g., Hosokawa et al. 2011; Hirano et al. 2014), it takes 0.84 and 0.73 Gyr for their remnant BHs of 100 and $1000 M_{\odot}$, respectively, to reach the mass of the $z = 7.1$ SMBH, $2 \times 10^9 M_{\odot}$, via the Eddington-limited accretion. These growth time scales are still exceeding (for seed BHs of $100 M_{\odot}$) or only slightly below (for $1000 M_{\odot}$ seeds) the age of the Universe at that time, 0.77 Gyr. Even in the latter case, the BH is required to continuously accrete at the Eddington rate all the way to the SMBH, i.e., the 100 % duty cycle in the six orders of magnitude in mass, which is quite improbable both from the observational and theoretical points of view. From the high- z QSO observations, the duty cycle is estimated as $\lesssim 60$ % at most at $z \geq 3.5$ (e.g., Shen et al. 2007; Shankar et al. 2010). Theoretically, radiative feedback from the BH will make the growth time longer, so that the situation becomes

* E-mail: nakauchi@astr.tohoku.ac.jp

† Hamamatsu Professor

even worse (e.g., Alvarez et al. 2009; Milosavljević et al. 2009), although the super-Eddington accretion, if it occurred, may help shorten the growth time enormously (e.g., Volonteri & Rees 2005; Alexander & Natarajan 2014).

The so-called direct collapse scenario is an alternative pathway. In this framework, we suppose that a supermassive star (SMS) of $\sim 10^5 M_\odot$ forms from metal-free gas in the early Universe and collapses directly to a BH with almost the same mass by the post-Newtonian instability (e.g., Shapiro & Teukolsky 1983). With the more massive seeds, the growth time to $\sim 2 \times 10^9 M_\odot$ is reduced to < 0.5 Gyr, below the age of the Universe at $z = 7.1$ by some margin.

In a currently favored scenario (Bromm & Loeb 2003), the SMSs are supposed to be formed in atomic-cooling halos where the H_2 formation is prohibited either by photodissociation due to strong far-ultraviolet radiation (Omukai 2001; Wolcott-Green et al. 2011; Sugimura et al. 2014) or collisional dissociation by a high-density shock (Inayoshi & Omukai 2012). In such halos, a cloud collapses isothermally at ~ 8000 K solely by the atomic cooling (Omukai 2001). Without a major episode of cooling, the cloud collapses monolithically avoiding significant fragmentation until the formation of a protostar at its center (Inayoshi et al. 2014; Becerra et al. 2015). The high temperature in the pre-stellar cloud results in the high accretion rate of $\dot{M}_{\text{acc}} = 0.1\text{--}1 M_\odot \text{ yr}^{-1}$ onto the protostar according to the relation $\dot{M}_{\text{acc}} \sim c_s^3/G$ (e.g., Shu 1977). Note that even a tiny amount of metals induces significant fragmentation in the collapsing gas cloud, so that SMS formation can proceed only in the metal-free environment (Omukai et al. 2008).

Such rapid accretion must be maintained until the central protostar grows to $\gtrsim 10^5 M_\odot$ by circumventing the possible obstacles. For example, in the case of the formation of ordinary first stars, radiative feedback, including the photoevaporation of the accretion flows, plays an important role in terminating their accretion growth and setting the final mass at a few $10\text{--}100 M_\odot$ (e.g., McKee & Tan 2008; Hosokawa et al. 2011, 2016; Susa 2013). But, this is not the case for the SMS formation. With the accretion rate exceeding a threshold value, $0.03 M_\odot \text{ yr}^{-1}$, the protostellar evolution changes completely (Hosokawa et al. 2012, 2013). Once the protostellar luminosity becomes close to the ‘‘classical’’ Eddington luminosity, $L_{\text{Edd,es}} = 4\pi cGM_*/\kappa_{\text{es}}$ where κ_{es} is the Thomson scattering opacity, at a few $10 M_\odot$, the stellar envelope swells greatly in radius reaching as large as $10\text{--}100$ AU. With the stellar effective temperature as low as ~ 5000 K, UV photons are hardly emitted and radiative feedback is too weak to halt the accretion. Resembling the present-day red super-giant stars in appearance, the name ‘‘super-giant protostars’’ (SGPSs) is coined for the rapidly accreting stars with the bloated envelopes. It is also known that the pulsational mass-loss rates from SGPSs are at most $\sim 10^{-3} M_\odot \text{ yr}^{-1}$, two or three orders of magnitude lower than the accretion rate (Inayoshi et al. 2013). Thus the pulsation either would not prevent them growing supermassive.

A radiation driven stellar wind is another possible obstacle for the SGPS growth. Similarly to the local Wolf-Rayet (WR) stars, which exhibit the mass-loss at the rates of $\dot{M}_w \sim 10^{-5}\text{--}10^{-4} M_\odot \text{ yr}^{-1}$ in radiation-driven winds (Gräfener et al. 2012), the SGPSs have luminosities close to the classical Eddington value. In addition, the SG-

PSs have a layer of density inversion, where the density increases outwardly, near the surface. Although the radiative luminosity locally exceeds the Eddington value $L_{\text{Edd,local}} = 4\pi cGM_*/\kappa$, where κ is the local opacity (Hosokawa et al. 2012, 2013), the hydrostatic equilibrium is still achieved as the layer is pushed down by the weight of the outer dense layers (e.g., Joss et al. 1973). If we omit the assumption of hydrostatic equilibrium and allow the matter to flow, however, we may find a wind solution blowing from the stellar surface (Ro & Matzner 2016). If such a stellar wind causes the significant mass loss, the stellar mass growth via accretion may be stopped at some moment before the formation of a SMS. To examine such a possibility, we here construct steady stellar wind solutions launched from the surface of SGPSs assuming the spherical symmetry. We find that the radiation pressure force in fact allows the smooth acceleration from the subsonic to supersonic regime. The wind velocity, however, does not reach the stellar escape velocity since the acceleration is suddenly over due to the opacity cutoff below $\sim 10^4$ K. We thus conclude that the stellar wind either does not prevent the growth of a SGPS and it will eventually grow to a SMS as long as the rapid accretion is maintained.

The rest of this paper is organized as follows. In Section 2, we describe the basic equations and the method to construct the stellar wind models. In Section 3, we construct a series of wind solutions passing through the sonic point smoothly, without considering the connection to the stars at their bases and classify the solutions. In Section 4, we present the wind solutions connected to the SGPSs and examine whether the wind mass-loss occurs from the SGPSs. Finally, Section 5 is devoted to the summary and discussion.

2 FORMULATION OF OPTICALLY THICK WIND SOLUTIONS

In this section, we describe the basic equations and boundary conditions to calculate the stellar wind solutions from SGPSs. In Figure 1, we illustrate the situation considered here. We suppose that the SGPS is composed of metal-free gas and gains the mass through the geometrically thin accretion disk. Except for the equatorial region, stellar winds could be launched from the surface by the radiation pressure force. We do not consider the interaction between the accretion disk and the wind, for simplicity. Assuming that the accretion region is small in comparison with the outflowing region, we consider the steady wind structure under the assumption of the spherical symmetry.

2.1 Basic Equations

We focus on the formulation valid for the optically thick winds (Finzi & Wolf 1971; Żytkow 1972; Quinn & Paczynski 1985; Lee 1990; Kato & Iben 1992; Kato & Hachisu 1994; Nugis & Lamers 2002; Dotan & Shaviv 2012; Ro & Matzner 2016), which is equivalent to assuming that the wind acceleration occurs beneath the photosphere as in the case of the dense WR wind (e.g., Crowther 2007). The basic equations governing the wind structure are as follows.

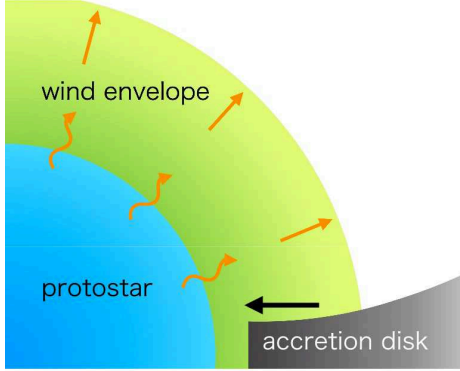


Figure 1. Schematic picture of the stellar winds launched from the accreting SGPSs.

First, the equations of motion (EoM) and continuity (EoC) are

$$v \frac{dv}{dr} + \frac{1}{\rho} \frac{dP}{dr} + \frac{GM_*}{r^2} = 0, \quad (1)$$

$$\dot{M}_{\text{wind}} \equiv 4\pi r^2 \rho v = \text{const.}, \quad (2)$$

where G is the gravitational constant, M_* the total stellar mass, \dot{M}_{wind} the mass outflow rate, and v, P , and ρ correspond to the velocity, total pressure, and density at radius r , respectively. Since the radiation field is the thermal black body in good approximation, the radiation pressure is given by $P_{\text{rad}} = aT^4/3$, where a is the radiation constant, and T the temperature. The total pressure P is given by the sum of the gas pressure P_{gas} and the radiation pressure P_{rad} :

$$P = P_{\text{gas}} + P_{\text{rad}} = \frac{\mathcal{R}}{\mu} \rho T + \frac{1}{3} a T^4, \quad (3)$$

where \mathcal{R} is the gas constant, and $\mu = \mu(\rho, T)$ the mean molecular weight. We consider metal-free gas, composed of H and He with the mass fractions of $X = 0.7$ and $Y = 0.3$, respectively. The mean molecular weight μ varies with the ionization degrees of H, He, and He^+ in the wind. After integration with respect to r , the energy equation is

$$\Lambda \equiv L_{\text{rad}} + \dot{M}_{\text{wind}} \left(\frac{v^2}{2} + w_{\text{gas}} + w_{\text{rad}} - \frac{GM_*}{r} \right) = \text{const.}, \quad (4)$$

where $w_{\text{gas}} = e_{\text{gas}} + P_{\text{gas}}/\rho$ is the specific enthalpy of the gas, with e_{gas} the specific internal energy of the gas including the ionization energy of H, He, and He^+ , and $w_{\text{rad}} = 4aT^4/3\rho$ that of radiation, respectively. The radiative luminosity in

the fluid frame L_{rad} is calculated by the diffusion approximation:

$$L_{\text{rad}} = -\frac{16\pi a c r^2 T^3}{3\kappa\rho} \frac{dT}{dr}, \quad (5)$$

where c is the speed of light, and κ the Rosseland mean opacity. For the Rosseland mean opacity, we use the tabulated values from the OPAL project (Iglesias & Rogers 1996) and from Alexander & Ferguson (1994) above and below 7000 K, respectively.

In Eqs. (1-5), we have four unknown functions, $v(r), \rho(r), T(r)$, and $L_{\text{rad}}(r)$. A wind solution can be obtained with the proper boundary conditions provided, which we describe in the next subsection.

2.2 Boundary Conditions

We impose the boundary conditions at the sonic point r_s and at the matching point r_m of the star and the wind. The latter corresponds to the base of the wind.

2.2.1 Condition at the Sonic Point

The sonic point corresponds to the singular point of the EoM (Eq. 1). Eq. (1) can be rewritten in a form that explicitly shows the presence of the singular point, by substituting the EoC (Eq. 2) and the EoS (Eq. 3) into Eq. (1):

$$\frac{1}{v} \frac{dv}{dr} = \left[\frac{2}{r} c_{\text{T}}^2 - \frac{1}{\rho} \left(\frac{\partial P_{\text{gas}}}{\partial T} \right)_{\rho} \frac{dT}{dr} + \frac{GM_*}{r^2} (\Gamma_r - 1) \right] / (v^2 - c_{\text{T}}^2), \quad (6)$$

where $c_{\text{T}} = \sqrt{(\partial P/\partial \rho)_T}$ is the isothermal sound speed, and $\Gamma_r \equiv L_{\text{rad}}/L_{\text{Edd}}$ the Eddington ratio.

In the wind solutions, the numerator of Eq. (6) should vanish simultaneously at the sonic point, since the velocity gradient is required to be finite there (Lamers & Cassinelli 1999). This gives us the following boundary condition:

$$\Gamma_r = \frac{1 - \left(\frac{2c_{\text{T}}}{v_{\text{esc}}} \right)^2}{1 + \left(\frac{\partial P_{\text{gas}}}{\partial P_{\text{rad}}} \right)_{\rho}} \text{ at } v = c_{\text{T}}, \quad (7)$$

where $v_{\text{esc}} \equiv \sqrt{2GM_*/r}$ is the escape velocity at radius r .

We obtain a unique stellar wind solution for each set of radius, density, and temperature (r_s, ρ_s, T_s) at the sonic point. The velocity v_s and the radiation luminosity $L_{\text{rad},s}$ at the sonic point are evaluated by using the first boundary condition (Eq. 7) as $v_s = c_{\text{T}}(\rho_s, T_s)$ and $L_{\text{rad},s} = L_{\text{rad}}(r_s, \rho_s, T_s)$, respectively. Substituting the evaluated values of v_s and $L_{\text{rad},s}$ into Eqs. (2) and (4), we can fix \dot{M}_{wind} and Λ , which remain constant throughout a wind solution. The velocity gradient at the sonic point is obtained by applying the de l'Hopital rule to Eq. (6) (Lamers & Cassinelli 1999; Nugis & Lamers 2002). The above procedure allows us to construct one wind solution that smoothly passes through the sonic point.

2.2.2 Conditions at the Matching Point of Star and Wind

We impose another boundary condition at the base of the stellar wind to connect physical quantities continuously from

the star to the wind. We assume that the wind starts blowing at some radius r_m . We regard r_m as a free parameter without specifying how the wind initially arises in the atmosphere. For a hydrostatic stellar model, we set the matching point from a layer that satisfies the following two conditions. First, we require that the mass contained between the matching and the sonic radii is small and less than 5 % of the stellar mass. This is because the mass is taken as a constant and equal to the stellar one in the gravity term of the wind equation. Second, we require that, around the matching radius, the energy generation either via nuclear burning or gravitational contraction is negligible and the total luminosity becomes constant in radius ($L_r \sim \text{const.}$).

For the boundary conditions, we first require that the density and temperature are continuous across the matching point r_m :

$$\rho(r_m) = \rho_*(r_m) \text{ and } T(r_m) = T_*(r_m). \quad (8)$$

where the subscript $*$ indicates the quantities from the (hydrostatic) stellar model. Note that the wind velocity is highly subsonic at r_m as long as $r_m \ll r_s$. The first term in Eq. (1) thus being much smaller than the second term, i.e., $v|dv/dr| \ll \rho^{-1}|dP_{\text{gas}}/dr|$, so that the gas is almost in the hydrostatic equilibrium around r_m , i.e., the density and temperature of the wind asymptotically approach those of the hydrostatic stellar model. Second, without the energy source in the envelope, the energy flux must be continuous across r_m :

$$\begin{aligned} L_*(r_m) &= \left[L_{\text{rad}} + \dot{M}_{\text{wind}} \left(\frac{v^2}{2} + w_{\text{gas}} + w_{\text{rad}} \right) \right]_{r_m} \\ &= \Lambda + \frac{GM_*}{r_m} \dot{M}_{\text{wind}}, \end{aligned} \quad (9)$$

where $L_*(r_m)$ is the total luminosity of the star at r_m . Eq. (9) indicates that at the matching radius, r_m , a fraction of the luminosity in the hydrostatic envelope, $L_*(r_m)$, is converted into the wind kinetic energy and the internal energy advected with the bulk motion of the flow. This leads to discontinuities in the gradients of temperature and density as well as in the radiation luminosity at r_m .

2.2.3 Constructing the Wind Solution Connected to a Stellar Model at a Matching Point

With our four boundary conditions, one at the sonic point and three at the matching point, we can find four unknown functions $v(r)$, $\rho(r)$, $T(r)$, and $L_{\text{rad}}(r)$ to construct a stellar wind solution continuously connected to the hydrostatic model.

The numerical integration is performed in the following way. For a given matching point r_m , we obtain the total luminosity $L_*(r_m)$ from the hydrostatic stellar model. We guess the density and temperature at the sonic point (ρ_s , T_s) and find the sonic radius r_s by using the boundary condition Eq. (9) with $L_*(r_m)$. Then, we integrate Eqs. (1-5) numerically inward from r_s to r_m . This is repeated with improving the guess for (ρ_s , T_s) until the two boundary conditions at r_m (Eq. 8) are satisfied. At this moment, we obtain a unique wind solution in the subsonic region, as well as the constants of the motion, \dot{M}_{wind} and Λ . The structure in the outer supersonic region can be solved as an initial value problem from the sonic point determined in the procedure above.

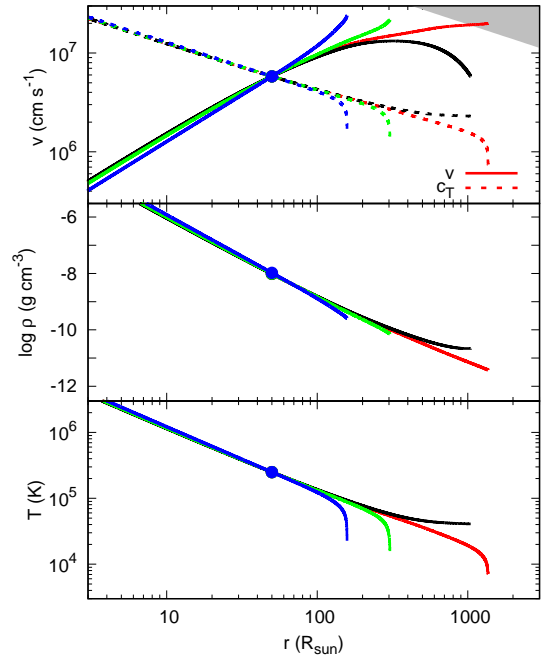


Figure 2. Stellar wind solutions for $M_* = 100 M_\odot$, $T_s = 2.5 \times 10^5$ K, and $r_s = 50 R_\odot$. In each panel, black, red, green, and blue lines correspond to $\rho_s = 9.65, 9.71, 9.85$, and 10.5×10^{-9} g cm $^{-3}$, respectively. The velocity (upper), density (middle) and temperature profiles (lower) are shown. The filled circle in each panel indicates the sonic point. In the upper panel, the isothermal sound speed c_T (dashed) is also shown and the grey-shaded region indicates velocities exceeding the local escape velocity v_{esc} .

Eqs. (1-5) are solved by the explicit first-order Euler method. The grid spacing is calculated from $\Delta r = \epsilon \times \min(T/|dT/dr|, v/|dv/dr|)$. We adopt $\epsilon = 10^{-4}$ as a fiducial value. We have confirmed that our results do not change with further reducing ϵ .

3 CLASSIFICATION OF WIND SOLUTIONS

In this section, before discussing the proper wind solutions connected to the hydrostatic stellar model at the matching point, we see the general features of wind solutions. For this purpose, we here calculate a wind solution passing through the sonic point for each given set of (r_s , ρ_s , T_s), and do not try to make it connect to the hydrostatic solution (see Section 2).

In Figure 2, we illustrate the stellar wind solutions for $M_* = 100 M_\odot$, $T_s = 2.5 \times 10^5$ K, $r_s = 50 R_\odot$ ¹, and four different values of density $\rho_s = 9.65, 9.71, 9.85, 10.5 \times 10^{-9}$ g cm $^{-3}$. The velocity (top), density (middle), and temperature (bottom) profiles are shown. For the different values of ρ_s , the structure in the subsonic region is similar to

¹ We here adopt a very small sonic radius $r_s \sim 50 R_\odot$ to compare the properties of the successful wind solution with those of the stalled one. If we adopt as large sonic radius ($r_s \sim 2500 R_\odot$) as in the next section, we find that only stalled solutions are obtained.

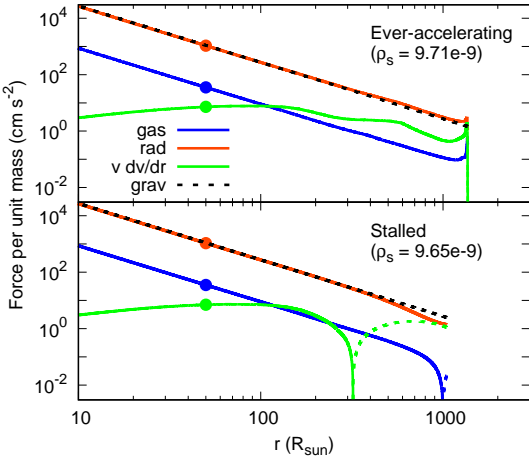


Figure 3. Force balance in the wind region: the radiation pressure gradient (red), gas pressure gradient (blue), acceleration term (green), and gravity (black). Shown is the case for $M_* = 100 M_\odot$, $T_s = 2.5 \times 10^5$ K, and $r_s = 50 R_\odot$. Depending on the density at the sonic point ρ_s , the type of the wind solution changes: (*upper*; ever-accelerating solution) the case of $\rho_s = 9.71 \times 10^{-9} \text{ g cm}^{-3}$, (*lower*; stalled solution) $\rho_s = 9.65 \times 10^{-9} \text{ g cm}^{-3}$. Dashed lines show that the force is in the negative (inward) direction.

each other. On the other hand, the structure in the supersonic region largely differs, which allows us to classify the solutions into the following two types:

i) *stalled wind solution:*

In some solutions, for example that with $\rho_s = 9.65 \times 10^{-9} \text{ g cm}^{-3}$, the velocity reaches the maximum at some radius and then decreases monotonically. We call this type of solutions as the stalled wind solutions. In this case, we stop the integration when the Mach number falls below 1.5.

ii) *ever accelerating wind solution:*

In some solutions, for example other cases ($\rho_s \geq 9.71 \times 10^{-9} \text{ g cm}^{-3}$) shown in Figure 2, the velocity continues increasing monotonically up to $\sim 200 \text{ km s}^{-1}$. We call this type of solutions as the ever accelerating wind solution. In this case, we stop the integration at the photosphere, which is defined as the radius where the temperature becomes equal to the effective temperature $T_{\text{eff}} = (L_{\text{rad}}/4\pi r^2 \sigma_{\text{SB}})^{1/4}$, since our formalism is only valid in the optically thick regime, i.e., inside the photosphere.

Figure 3 shows the force balance for the two types of the solutions $\rho_s = 9.65 \times 10^{-9} \text{ g cm}^{-3}$ (lower panel; stalled solution) and $9.71 \times 10^{-9} \text{ g cm}^{-3}$ (upper panel; ever accelerating solution). In the subsonic region, the acceleration term is much smaller than the total (gas and radiation) pressure gradient, i.e., the hydrostatic equilibrium holds well, in both cases. Using the equation of hydrostatic equilibrium

$$\frac{1}{\rho} \frac{dP_{\text{gas}}}{dr} = \frac{GM_*}{r^2} (\Gamma_r - 1), \quad (10)$$

and the fact that the Eddington ratio Γ_r is almost constant because of the constancy of the opacity and radiative luminosity there, we can derive the power-law distributions

$\rho \propto r^{-3}$ and $T \propto r^{-1}$ seen in Figure 2. We also obtain $v \propto r$ from these relations and Eq. (2).

The wind structure in the supersonic region differs greatly among the stalled and ever-accelerating solutions. In the stalled solution (Figure 3 lower), the outward pressure gradient has fallen below the inward pull of gravity already at $\sim 300 R_\odot$, so that the wind decelerates monotonically beyond this point. On the other hand, in the ever accelerating solution (Figure 3 upper), the acceleration continues until $\gtrsim 1000 R_\odot$ and reaches the velocity $\sim 200 \text{ km s}^{-1}$ at the photosphere, exceeding the escape velocity. In this case, the wind is successfully launched with the mass-loss rate of $\dot{M}_{\text{wind}} \sim 0.14 M_\odot \text{ yr}^{-1}$.

It should be noted, however, that not all the ever-accelerating solutions can be regarded as “successful” winds. For example, for $\rho_s = 9.85$ and $10.5 \times 10^{-9} \text{ g cm}^{-3}$, although being continuously accelerated, the solution reaches the photosphere before the velocity exceeds the escape value. Outside the photosphere, the further acceleration is improbable for the gas with the primordial composition (see the discussion), and the matter in the wind would eventually fall back to the star. Hence, the failure of some ever-accelerating solutions to launch the wind comes from the limited acceleration regime due to the small photospheric radii.

The successful wind solution has the most extended photosphere among the ever-accelerating solutions. The maximum value for the photospheric radius can be estimated from the argument that the luminosity does not exceed the classical Eddington limit $L_{\text{Edd,es}}$ and the effective temperature does not fall below $T_{\text{eff}} \sim 5000 \text{ K}$ due to the sharp opacity cutoff at lower temperatures:

$$\begin{aligned} r_{\text{ph}} &= (L_{\text{ph}}/4\pi\sigma_{\text{SB}}T_{\text{eff}}^4)^{1/2} \\ &\lesssim (L_{\text{Edd,es}}/4\pi\sigma_{\text{SB}}T_{\text{eff}}^4)^{1/2} \\ &\lesssim r_{\text{ph,max}} \equiv 2160 R_\odot (M_*/100 M_\odot)^{1/2} (T_{\text{eff}}/5000 \text{ K})^{-2}. \end{aligned} \quad (11)$$

This value is consistent with our numerical result for $\rho_s = 9.71 \times 10^{-9} \text{ g cm}^{-3}$ with $r_{\text{ph}} \sim 1400 R_\odot$ (red line, Figure 2 middle).

We find that there is an upper limit on the stellar mass for the successful wind solutions to be found. In these solutions, the velocity at the photosphere v_{ph} must be larger than the escape velocity there:

$$v_{\text{ph}} \geq v_{\text{esc}}(r_{\text{ph}}). \quad (12)$$

From experiments, we found that the velocity at the photosphere v_{ph} is almost solely determined by T_s ($v_{\text{ph}} \sim 200 \text{ km s}^{-1}$ for our choice of $T_s = 2.5 \times 10^5 \text{ K}$ here) and increases with T_s . Since they correspond to the solutions of the maximum photospheric radius, by substituting Eq. (11) into Eq. (12), we obtain the upper limit on the mass of a star that can successfully launch the wind for a given T_s , i.e., v_{ph} :

$$M_* \simeq 200 M_\odot (v_{\text{ph}}/200 \text{ km s}^{-1})^4 (T_{\text{eff}}/5000 \text{ K})^{-4}. \quad (13)$$

For example, for $T_s = 2.5 \times 10^5 \text{ K}$ ($v_{\text{ph}} \sim 200 \text{ km s}^{-1}$), the successful wind solutions exist only up to $M_* \simeq 200 M_\odot$.

4 WIND SOLUTIONS CONNECTED WITH THE HYDROSTATIC STARS

In this section, we see whether SGPSs have the wind solutions with the terminal velocity exceeding the escape value. We construct the solutions as described in Section 2.2, i.e., by connecting the outer wind and inner hydrostatic solutions at the matching point. As for the hydrostatic solutions, we adopt our previous results of Hosokawa et al. (2013), who followed the protostellar evolution until the stellar mass reaches 10^4 - $10^5 M_\odot$ at the constant accretion rates in the range $\dot{M}_{\text{acc}} = 0.1$ - $1.0 M_\odot \text{ yr}^{-1}$. They showed that such protostars, whose structures are calculated under the assumption of hydrostatic equilibrium, have very extended envelopes. Below, we show that an outer part of the envelope can also take the outflowing structure, where the gas is not in the hydrostatic balance.

We first see the wind solutions for SGPSs accreting at $\dot{M}_{\text{acc}} = 0.1 M_\odot \text{ yr}^{-1}$ in Section 4.1 and then the cases with the higher accretion rate $\dot{M}_{\text{acc}} = 1.0 M_\odot \text{ yr}^{-1}$ in Section 4.2. In the former case, the stellar models are available only up to the mass reaches $M_* \sim 10^4 M_\odot$, while in the latter case, up to $M_* \sim 10^5 M_\odot$. Hence, for SGPSs more massive than $\sim 10^4 M_\odot$, wind solutions can be examined only in the latter case.

4.1 Cases with $\dot{M}_{\text{acc}} = 0.1 M_\odot \text{ yr}^{-1}$

4.1.1 $M_* = 100 M_\odot$ SGPS

Hosokawa et al. (2013) showed that, at this accretion rate, by the time the stellar mass reaches $100 M_\odot$ the protostar already has the extended envelope of $R_* \simeq 2000 R_\odot$, characteristic to the SGPSs. If the mass loss is vigorous enough to prevent the stellar growth at this early stage of the SGPSs, the star cannot reach the supermassive regime $M_* \sim 10^4$ - $10^5 M_\odot$. We thus study the case of $M_* = 100 M_\odot$, before considering the more massive regime in Section 4.1.3. Here, the matching point r_m is taken outside $1300 R_\odot$, which encompasses more than 95 % of the total mass.

In Figure 4, we show the wind solution with the matching point at $r_m = 1700 R_\odot$ (the filled square). The velocity, density and temperature profiles are presented in the top, middle and bottom panels, respectively. The flow is initially subsonic with the Mach number < 0.1 around the matching point and then becomes supersonic at $r_s \simeq 2600 R_\odot$. The flow, however, decelerates after taking the maximum velocity at $\simeq 2700 R_\odot$, i.e., it is the stalled solution. The wind solution (red solid) has the more extended structure with the lower density than in the hydrostatic model (black dashed). Note that, unlike the hydrostatic case having the density inversion around $r = 2000 R_\odot$, the wind solution does not have such a structure and the flow is just accelerated by the radiation pressure.

Figure 5 shows the radial distributions of the Rosseland mean opacity κ (upper panel) and the local Eddington ratio Γ_r (lower panel). The radiative luminosity remains sub-Eddington, i.e., $\Gamma_r < 1$, throughout the subsonic region. Around the opacity bump at $\simeq 2700 R_\odot$ due to the bound-free absorption of H atoms and H^- ions, a thin super-Eddington layer appears just outside the sonic point. The sharp drop of the opacity caused by the hydrogen recom-

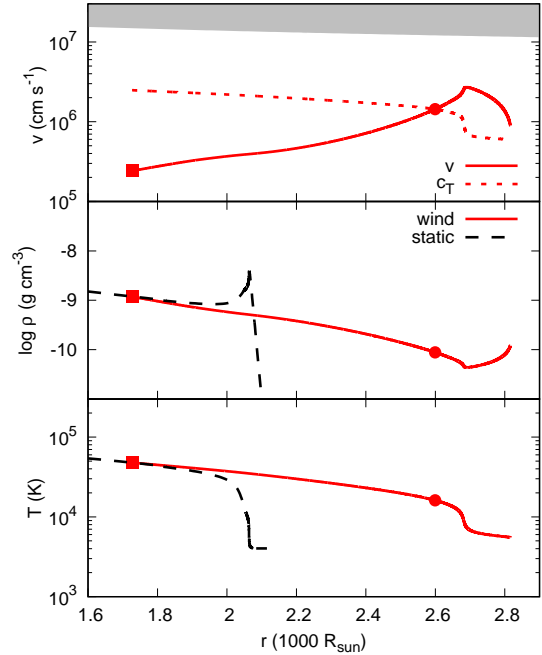


Figure 4. The wind solution for $\dot{M}_{\text{acc}} = 0.1 M_\odot \text{ yr}^{-1}$ and $M_* = 100 M_\odot$, with the matching point at $r_m = 1700 R_\odot$ (the filled square). In the upper panel, the wind velocity (solid) is shown along with the isothermal sound speed (dotted). The upper grey-shaded region indicates the region where velocity exceeds the local escape velocity. The middle and lower panels show the density and temperature profiles, respectively. Also shown in these panels are the profiles for the hydrostatic star (dashed).

bination below 10^4 K, however, pushes back the Eddington ratio below unity again for $r \gtrsim 2700 R_\odot$.

Figure 6 shows the force balance for this case. We see that the radiation pressure (red) dominates the gas pressure (blue) everywhere. Since the pressure gradient is almost in balance with the gravity (black), hydrostatic equilibrium still holds approximately in the subsonic region. The acceleration term (green) gradually increases outward and takes the maximum in the supersonic region at $r \simeq 2700 R_\odot$. However, the acceleration term then declines dramatically in the outer region owing to the decrease of the radiation pressure force, which is in proportion to the opacity κ .

4.1.2 Dependence on the Matching Radius

Next, we investigate how the wind structure changes by varying the matching radius r_m . Figures 7 and 8 present the wind solutions for the different matching radii with the same $M_* = 100 M_\odot$ SGPS model. In each figure, the blue, green, red, and black lines represent those with the different matching radii of $r_m = 1800, 1700, 1600$, and $1500 R_\odot$, respectively.

The upper panel of Figure 7 shows that the velocity structure is qualitatively similar to each other even with the different matching radii: the flow velocity increases and becomes supersonic at some point, but starts decreasing before exceeding the escape value. This is due to the sharp decrease

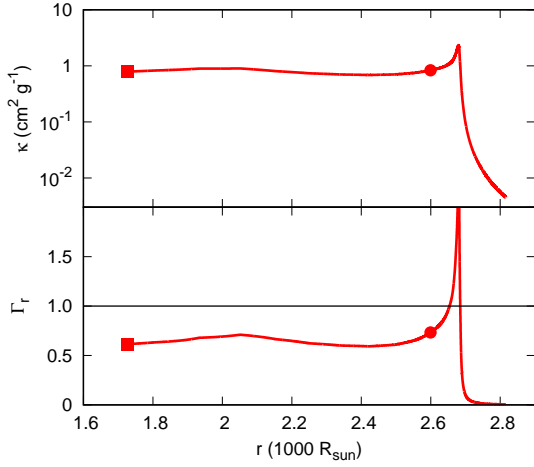


Figure 5. Radial distributions of the Rosseland mean opacity κ (upper) and the local Eddington ratio Γ_r (lower) for the wind solution with $\dot{M}_{\text{acc}} = 0.1 M_{\odot} \text{ yr}^{-1}$ and $M_* = 100 M_{\odot}$. The matching point (filled square) is located at $r_m = 1700 R_{\odot}$. The sonic point is indicated by the filled circle. Note that κ is shown using a log scale, whereas Γ_r is shown using a linear scale.

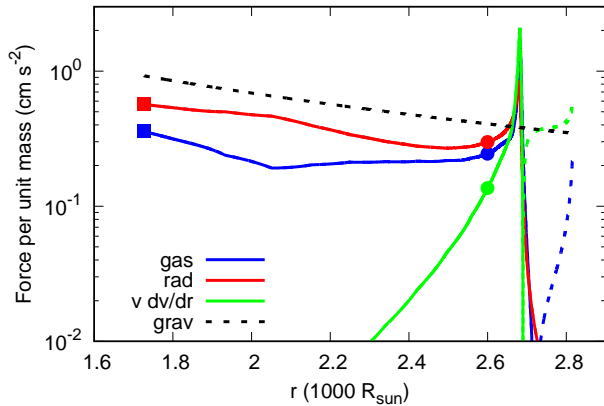


Figure 6. Same as Figure 3, but for the wind solution matched with the hydrostatic envelope: the radiation pressure gradient (red), gas pressure gradient (blue), acceleration term (green), and gravity (black). The dashed parts of the lines show that the force is in the negative (inward) direction. The stellar parameters are $\dot{M}_{\text{acc}} = 0.1 M_{\odot} \text{ yr}^{-1}$ and $M_* = 100 M_{\odot}$. The matching point (filled square) is located at $r_m = 1700 R_{\odot}$. The sonic point is indicated by the filled circle.

of the opacity and radiation force caused by the recombination of hydrogen (upper panel of Figure 8), as mentioned in Section 4.1.1.

With the smaller r_m , the flows have the mass-loss rates $\dot{M}_{\text{wind}} = 1.2, 0.83, 0.55, 0.42 M_{\odot} \text{ yr}^{-1}$, which could have a great impact on the stellar growth if the wind is successfully launched. All of them, however, belong to the stalled wind solutions, which implies that the steady wind is not launched from this stellar model regardless of the matching radius,

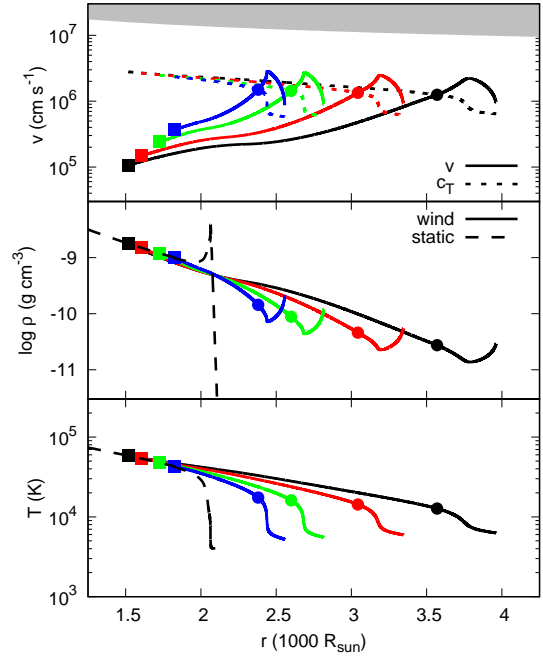


Figure 7. Effect of the different matching radius on the wind structure. Shown are the velocity (upper), density (middle), and temperature (lower) profiles for the solutions with the same stellar parameters $\dot{M}_{\text{acc}} = 0.1 M_{\odot} \text{ yr}^{-1}$ and $M_* = 100 M_{\odot}$ but with the different matching radii $r_m = 1800$ (blue), 1700 (green), 1600 (red), and $1500 R_{\odot}$ (black).

and that the stellar mass acquisition via accretion is thus not prevented by the wind mass loss.

In the middle panel of Figure 7, we can see that, with the smaller matching radius r_m , the outflowing envelope has the more extended structure with the lower density at the sonic point. On the other hand, the temperature at the sonic point, which is located just inside the opacity peak (see Figure 8 upper), is $\simeq 10^4$ K for all the cases (Figure 7 lower) because of the very strong temperature-dependence of the opacity around this value.

The maximum value of the local Eddington ratio $\Gamma_{r,\text{max}}$ is lower for the inner matching point case (Figure 8 lower). This is because the density above the sonic point $r > r_s$ becomes lower for the smaller r_m , which results in the lower opacity and thus the smaller $\Gamma_{r,\text{max}}$. In particular, $\Gamma_{r,\text{max}}$ never reaches unity for r_m smaller than $1500 R_{\odot}$.

4.1.3 Dependence on the Stellar Mass

Next, we examine the stellar wind solutions for more massive SGPSSs with the same accretion rate $\dot{M}_{\text{acc}} = 0.1 M_{\odot} \text{ yr}^{-1}$. The wind solutions for the 1000 and $10^4 M_{\odot}$ stars are shown in Figures 9 and 10, respectively. Both stellar models have the extended envelopes with the radii $R_* \simeq 7000 R_{\odot}$ ($1000 M_{\odot}$) and $18000 R_{\odot}$ ($10^4 M_{\odot}$). The 95 % of the total stellar mass is enclosed within $2000 R_{\odot}$ for the $1000 M_{\odot}$ model and $500 R_{\odot}$ for the $10^4 M_{\odot}$ model, respectively. The matching radii are chosen at $r_m = 6000, 5500, 5000,$ and $4500 R_{\odot}$ for

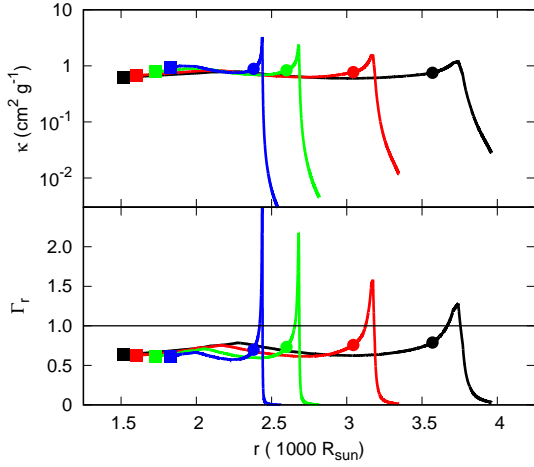


Figure 8. Profiles of the Rosseland mean opacity κ (upper) and the local Eddington ratio Γ_r (lower) for the wind solution with the same stellar parameters $\dot{M}_{\text{acc}} = 0.1 M_{\odot} \text{ yr}^{-1}$ and $M_* = 100 M_{\odot}$ but with the different values of the matching radii $r_m = 1800$ (blue), 1700 (green), 1600 (red), and 1500 R_{\odot} (black). Note that κ is shown using a log scale, whereas Γ_r is shown using a linear scale.

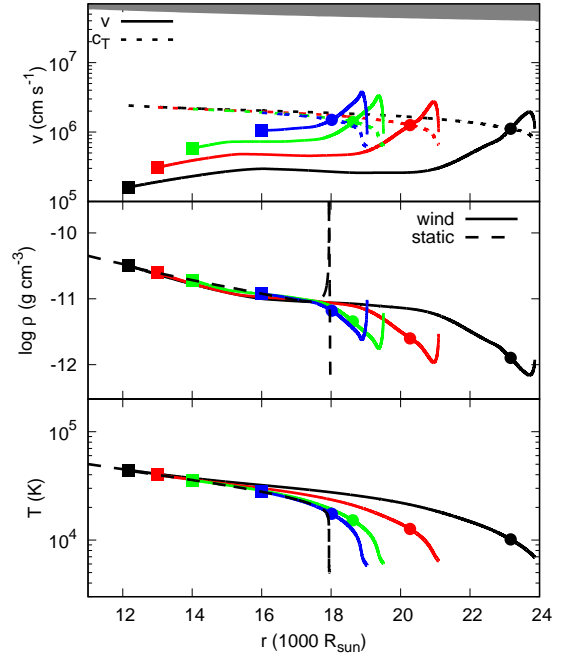


Figure 10. Same as Figure 7, but for the stellar model with $\dot{M}_{\text{acc}} = 0.1 M_{\odot} \text{ yr}^{-1}$ and $M_* = 10^4 M_{\odot}$. In each panel, the blue, green, red, and black lines correspond to the results for $r_m = 16000, 14000, 13000,$ and $12000 R_{\odot}$, respectively.

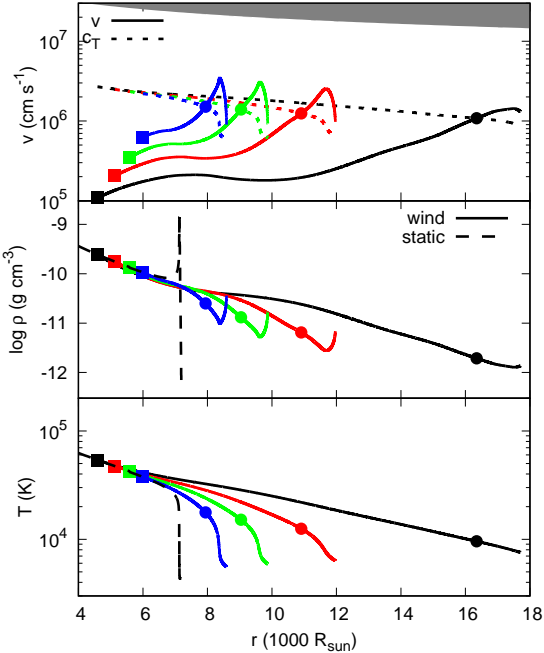


Figure 9. Same as Figure 7, but for the stellar model with $\dot{M}_{\text{acc}} = 0.1 M_{\odot} \text{ yr}^{-1}$ and $M_* = 1000 M_{\odot}$. In each panel, the blue, green, red, and black lines correspond to the results for $r_m = 6000, 5500, 5000,$ and $4500 R_{\odot}$, respectively.

1000 M_{\odot} , and $r_m = 16000, 14000, 13000,$ and $12000 R_{\odot}$ for $10^4 M_{\odot}$, respectively.

All these solutions for the 1000 and $10^4 M_{\odot}$ stars are again the stalled ones as in the case of the 100 M_{\odot} model: the flow starts to decelerate after reaching the sonic point without reaching the escape velocity. Note also that the maximum velocity in the wind remains much below the escape velocity $v_{\text{esc},*}$ for more massive models since the escape velocity increases with the stellar mass as $v_{\text{esc},*} \propto M_*^{1/4}$ from the relation $R_* \propto M_*^{1/2}$ for the SGPSs (Hosokawa et al. 2012). Whereas the mass-loss rates are mathematically determined as $\dot{M}_{\text{wind}} = 2.3, 1.4, 0.92, 0.54 M_{\odot} \text{ yr}^{-1}$ ($\dot{M}_{\text{wind}} = 3.1, 2.1, 1.3, 0.73 M_{\odot} \text{ yr}^{-1}$) for the 1000 M_{\odot} ($10^4 M_{\odot}$) models, such steady winds can not be launched from these stars and prevent the mass growth.

For the flow to be accelerated to the supersonic regime, the matching point must be located outside a certain radius, which is $r_{m,\text{min}} \simeq 4500 R_{\odot}$ ($12000 R_{\odot}$) for the $M_* = 1000 M_{\odot}$ ($10^4 M_{\odot}$) case. As seen in Figures 9 and 10, the velocity gradient at the sonic point becomes smaller for the smaller matching radius and it eventually becomes even negative below the threshold value $r_{m,\text{min}}$. In this case, the flow cannot reach the supersonic regime, so that we here consider only the case of $r_m > r_{m,\text{min}}$.

Hence, with the accretion rate of $\dot{M}_{\text{acc}} = 0.1 M_{\odot} \text{ yr}^{-1}$, the mass loss by stellar winds does not prevent SGPSs from growing up to at least $10^4 M_{\odot}$. Without more massive SGPS models, we can not examine the effect of stellar winds on the SGPS evolution for $M_* \geq 10^4 M_{\odot}$. We expect, however, that a SGPS reaches the supermassive regime, since successful

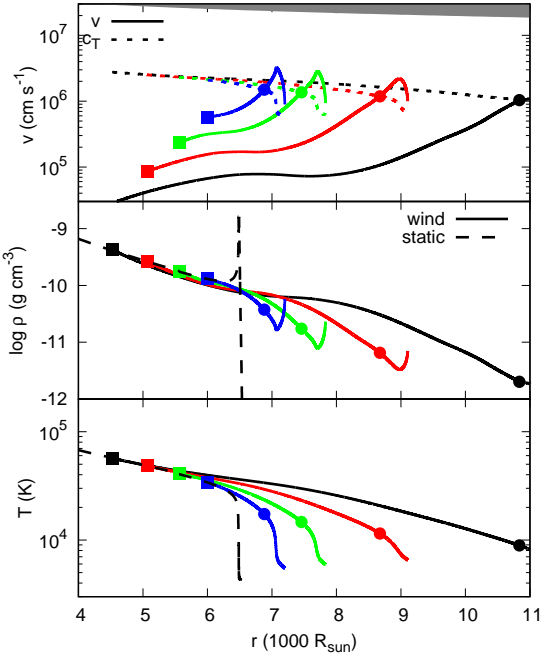


Figure 11. Same as Figure 7, but for the stellar model with $\dot{M}_{\text{acc}} = 1.0 M_{\odot} \text{ yr}^{-1}$ and $M_* = 1000 M_{\odot}$. In each panel, the blue, green, red, and black lines correspond to the results with $r_m = 6000, 5500, 5000,$ and $4500 R_{\odot}$, respectively.

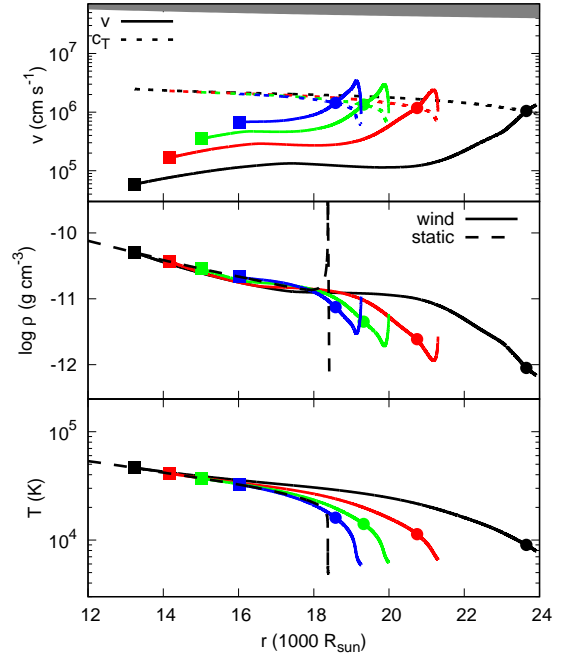


Figure 12. Same as Figure 7, but for the stellar model with $\dot{M}_{\text{acc}} = 1.0 M_{\odot} \text{ yr}^{-1}$ and $M_* = 10^4 M_{\odot}$. In each panel, the blue, green, red, and black lines correspond to the results with $r_m = 16000, 15000, 14000,$ and $13000 R_{\odot}$, respectively.

wind solutions exist only for $M_* \lesssim 200 M_{\odot}$, according to the analytical estimate in Section 3 (Eq. 13).

4.2 Cases with $\dot{M}_{\text{acc}} = 1.0 M_{\odot} \text{ yr}^{-1}$

Here, we consider the cases with the higher accretion rate of $\dot{M}_{\text{acc}} = 1.0 M_{\odot} \text{ yr}^{-1}$. In this case, the protostar becomes a SGPS when the stellar mass exceeds $\gtrsim 100 M_{\odot}$ (Hosokawa et al. 2013). Below, we show the results for the SGPS models with three different masses $M_* = 1000, 10^4,$ and $10^5 M_{\odot}$.

Figures 11 and 12 show the velocity, density, and temperature profiles of the wind solutions for the $M_* = 1000 M_{\odot}$ and $10^4 M_{\odot}$ models, respectively. They have the extended envelopes with the radii $R_* \simeq 6500 R_{\odot}$ ($1000 M_{\odot}$) and $18000 R_{\odot}$ ($10^4 M_{\odot}$), and $\sim 95\%$ of the total stellar mass is encompassed within $3500 R_{\odot}$ ($1000 M_{\odot}$) and $4000 R_{\odot}$ ($10^4 M_{\odot}$), respectively. The matching radii are chosen at four different radii: $r_m = 6000, 5500, 5000,$ and $4500 R_{\odot}$ for $1000 M_{\odot}$ and $r_m = 16000, 15000, 14000,$ and $13000 R_{\odot}$ for $10^4 M_{\odot}$, respectively. If we take the matching radii below $r_{m,\text{min}} \sim 4500 R_{\odot}$ ($\sim 13000 R_{\odot}$) for the $1000 M_{\odot}$ ($10^4 M_{\odot}$) model, the velocity gradient at the sonic point would finally be negative, and supersonic wind solutions can not be found, as we discuss in Sections 4.1.2 and 4.1.3.

The wind solutions have both quantitatively and qualitatively similar structures as those with the lower accretion rate $\dot{M}_{\text{acc}} = 0.1 M_{\odot} \text{ yr}^{-1}$ (c.f., Figures 9 and 10). They have almost the same values for the mathematically determined mass-loss rates, as

well: $\dot{M}_{\text{wind}} = 2.6, 1.3, 0.56, 0.24 M_{\odot} \text{ yr}^{-1}$ ($\dot{M}_{\text{wind}} = 3.6, 2.2, 1.2, 0.50 M_{\odot} \text{ yr}^{-1}$) for the $1000 M_{\odot}$ ($10^4 M_{\odot}$) model. This is because the SGPS models at the same mass have the similar envelope structures and radii regardless of the accretion rates. They are all classified into the stalled wind solution, i.e., wind acceleration is stopped before reaching the escape velocity in the supersonic region, and the flow can not escape from the system steadily. Hence, SGPSs can grow up to $10^4 M_{\odot}$ without being interrupted by stellar winds.

Finally in Figure 13, we show the wind solutions which are obtained for the $M_* = 10^5 M_{\odot}$ model. This SGPS model has a radius of $R_* \sim 29000 R_{\odot}$, and $\sim 95\%$ of the mass is enclosed within $\sim 2500 R_{\odot}$. The cases with the matching radii at $r_m = 26000$ and $25000 R_{\odot}$ are shown. Unlike all the wind solutions discussed so far, the radial extent of these wind solutions is shorter than the photospheric radius of the original hydrostatic SGPS model. They have the largest mass-loss rates: $\dot{M}_{\text{wind}} = 4.0, 2.3 M_{\odot} \text{ yr}^{-1}$. In these cases, again, the flows are classified into the stalled wind solution and fail to steadily escape from the gravitational pull of the star. In conclusion, with the higher accretion rate of $\dot{M}_{\text{acc}} = 1.0 M_{\odot} \text{ yr}^{-1}$, the mass loss by the stellar wind does not prevent the growth of a SGPS via mass accretion at least until a $10^5 M_{\odot}$ SMS forms.

5 SUMMARY AND DISCUSSION

We have examined whether in the supergiant protostar (SGPS) phase, a rapidly accreting protostar with the pri-

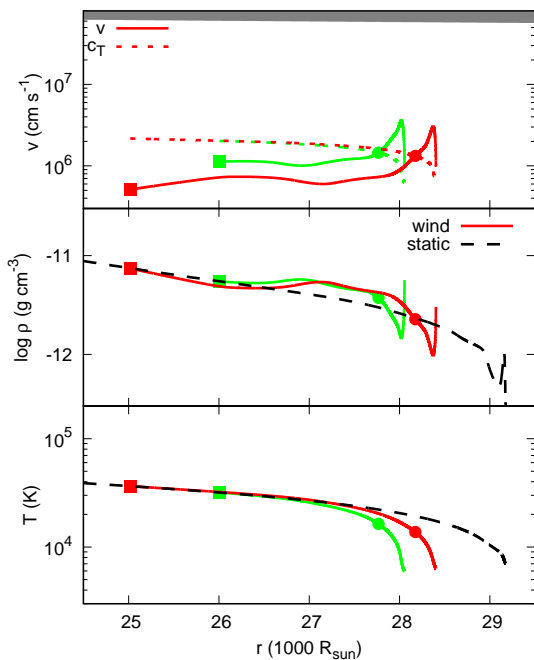


Figure 13. Same as Figure 7, but for the stellar model with $\dot{M}_{\text{acc}} = 1.0 M_{\odot} \text{ yr}^{-1}$ and $M_{*} = 10^5 M_{\odot}$. In each panel, the green and red lines correspond to the results with $r_{\text{in}} = 26000$ and $25000 R_{\odot}$, respectively. In this figure, the grey-shaded region show the region where $v \geq v_{\text{esc}}/2$ holds.

mordial composition has a steady optically thick wind that could cause such significant mass loss as to prevent the stellar mass growth. We have constructed the steady wind solutions which are continuously connected to the hydrostatic stellar envelopes. Our results show that the outflow stalls just after passing through the sonic point since the acceleration by radiation pressure becomes inefficient in the outermost part with temperature $\lesssim 10^4$ K, where the opacity sharply drops as hydrogen ions rapidly recombine. The flow velocity does not reach the stellar escape velocity in any of the cases. Hence, the growth of the SGPS mass via rapid accretion will not be hindered by strong mass loss at least until the SGPS mass reaches 10^4 - $10^5 M_{\odot}$.

Although the steady stellar wind is unlikely for the metal-free SGPSs, non-steady or sporadic mass loss might happen if we relax the assumption of the steady flow. This situation is similar to the wind solutions exceeding the so-called photon-tiring limit that sets the maximum rate of radiatively driven mass loss from hot massive stars (Owocki & Gayley 1997). In this case, a steady wind is not possible because the mass-loss rate is so high that the wind velocity never reaches the escape velocity even if all the stellar luminosity is expended for wind acceleration, and the wind necessarily stagnates at some radius. van Marle et al. (2009) performed one-dimensional radiation hydrodynamical (RHD) simulations to study the evolution of the photon-tired wind, and found that the sporadic outflow is in fact occasionally launched to escape from the stellar gravitational pull. However, there is a notable difference in our and their

winds. The opacity is always dominated by the Thomson scattering throughout their winds and remains at a constant value, while it drops sharply in the outermost part of the SGPS wind with $\lesssim 10^4$ K. Future time-dependent calculations are awaited to see the effects of non-steady winds for the SGPS cases.

The optically thick winds have originally been proposed to explain the substantial mass loss from WR stars (e.g., Kato & Iben 1992; Nugis & Lamers 2002; Ro & Matzner 2016). Note that our results here are consistent with the previous studies of the WR winds, although we have shown that the steady optically thick winds will be unimportant for the metal-free SGPSs. For instance, Ro & Matzner (2016) constructed the optically thick wind solutions that are connected to the hydrostatic WR structure at their bases, in the same way as our SGPS winds above. They showed that the outflow is accelerated by radiation pressure, in particular, in the region with temperature $\simeq 2 \times 10^5$ K, where the opacity takes the large values owing to a number of bound-bound transitions in iron (so-called the iron opacity “bump”). Nonetheless, none of their solutions achieves a high enough terminal velocity to exceed the stellar escape velocities, i.e., the outflow stalls as in our SGPS cases. They attributed this failure of reaching the escape velocity to their negligence of the contribution to opacity by the lines including the effect of velocity gradient, which enables more efficient momentum transport from radiation to matter (e.g., Castor et al. 1975). In metal-free SGPS cases, however, this line force, which is proportional to the number of available lines, would be negligible because the number of lines is very limited for the pure hydrogen and helium composition (Krtićka & Kubát 2006).

We have shown for the metal-free SGPSs that wind acceleration is rapidly quenched in the region of hydrogen recombination. With the solar composition, however, it would be maintained even for cool massive main-sequence stars for which the hydrogen recombination occurs in their atmosphere. This is due to the radiation pressure exerted through spectral lines of iron. Observations show such winds have smaller terminal velocities and higher mass-loss rates than those from hotter massive stars (the so-called bistability jump; e.g., Lamers et al. 1995). Therefore, this effect should be considered when we consider solar-metallicity wind models.

Multi-dimensional effects are known to be important in the surface layers of a massive star, where density inversion appears in the 1D hydrostatic model. For the solar composition, density inversion could be developed by the iron opacity bump, and the multi-dimensional structure of such layers was studied by Jiang et al. (2015) by way of the 3D local RHD simulations. They showed that these layers are convectively unstable and large density fluctuations give rise to a porous atmosphere, which is considered by some authors to play a key role in driving strong winds observed for WR stars and luminous blue variables (e.g., Shaviv 2000; van Marle et al. 2009). For SGPSs with the primordial composition, similar numerical simulations are needed, since density inversion is developed by the H and H^{-} opacity, and it is uncertain whether it leads to a porous atmosphere which might promote wind driving. Their calculation, however, was limited to the local patch of the stellar envelope, rather than encompassing the global wind structure, and so the resulting

mass-loss rate was not predicted. Therefore, global simulations are awaited to clarify the multi-dimensional effects on the wind driving in SGPS envelopes.

We have neglected any convective energy transport in the wind. We expect that this will not largely modify our results from the following consideration. In the supersonic regime, the convective energy flux is much less than the advected internal energy flux since the convection velocity is below the sound speed. In the subsonic regime, if we include the convective contribution, the radiative luminosity would be reduced for the constant total luminosity and so as the radiative acceleration of a wind. Therefore, the inclusion of convection should not change our conclusions that the steady wind is not driven from a SGPS.

ACKNOWLEDGMENTS

The authors thank K. Sugimura and T. Suda for fruitful discussions and T. Sakurai for providing us with the hydrostatic stellar models. This work is supported in part by the Grant-in-Aid from the Ministry of Education, Culture, Sports, Science and Technology (MEXT) of Japan, Nos.16J02951 (DN), 25800102, 15H00776 and 16H05996 (TH), 25287040 (KO), and 26400222 and 16H02168 (KN).

REFERENCES

- Alexander D. R., Ferguson J. W., 1994, *ApJ*, 437, 879
 Alexander T., Natarajan P., 2014, *Science*, 345, 1330
 Alvarez M. A., Wise J. H., Abel T., 2009, *ApJ*, 701, L133
 Becerra F., Greif T. H., Springel V., Hernquist L. E., 2015, *MNRAS*, 446, 2380
 Bromm V., Loeb A., 2003, *ApJ*, 596, 34
 Castor J. I., Abbott D. C., Klein R. I., 1975, *ApJ*, 195, 157
 Crowther P. A., 2007, *ARA&A*, 45, 177
 Dotan C., Shaviv N. J., 2012, *MNRAS*, 427, 3071
 Fan X., 2006, *NewAR*, 50, 665
 Finzi A., Wolf R. A., 1971, *A&A*, 11, 418
 Gräfener G., Owocki S. P., Vink J. S., 2012, *A&A*, 538, A40
 Haiman Z., 2013, in Wiklind T., Mobasher B., Bromm V., eds, *Astrophysics and Space Science Library* Vol. 396, *The First Galaxies*. p. 293 (arXiv:1203.6075), doi:10.1007/978-3-642-32362-1_6
 Hirano S., Hosokawa T., Yoshida N., Umeda H., Omukai K., Chiaki G., Yorke H. W., 2014, *ApJ*, 781, 60
 Hosokawa T., Omukai K., Yoshida N., Yorke H. W., 2011, *Science*, 334, 1250
 Hosokawa T., Omukai K., Yorke H. W., 2012, *ApJ*, 756, 93
 Hosokawa T., Yorke H. W., Inayoshi K., Omukai K., Yoshida N., 2013, *ApJ*, 778, 178
 Hosokawa T., Hirano S., Kuiper R., Yorke H. W., Omukai K., Yoshida N., 2016, *ApJ*, 824, 119
 Iglesias C. A., Rogers F. J., 1996, *ApJ*, 464, 943
 Inayoshi K., Omukai K., 2012, *MNRAS*, 422, 2539
 Inayoshi K., Hosokawa T., Omukai K., 2013, *MNRAS*, 431, 3036
 Inayoshi K., Omukai K., Tasker E., 2014, *MNRAS*, 445, L109
 Jiang Y.-F., Cantiello M., Bildsten L., Quataert E., Blaes O., 2015, *ApJ*, 813, 74
 Joss P. C., Salpeter E. E., Ostriker J. P., 1973, *ApJ*, 181, 429
 Kato M., Hachisu I., 1994, *ApJ*, 437, 802
 Kato M., Iben Jr. I., 1992, *ApJ*, 394, 305
 Krtićka J., Kubát J., 2006, *A&A*, 446, 1039
 Lamers H. J. G. L. M., Cassinelli J. P., 1999, *Introduction to Stellar Winds*
 Lamers H. J. G. L. M., Snow T. P., Lindholm D. M., 1995, *ApJ*, 455, 269
 Lee U., 1990, *MNRAS*, 244, 96
 McKee C. F., Tan J. C., 2008, *ApJ*, 681, 771
 Milosavljević M., Bromm V., Couch S. M., Oh S. P., 2009, *ApJ*, 698, 766
 Mortlock D. J., et al., 2011, *Nature*, 474, 616
 Nugis T., Lamers H. J. G. L. M., 2002, *A&A*, 389, 162
 Omukai K., 2001, *ApJ*, 546, 635
 Omukai K., Schneider R., Haiman Z., 2008, *ApJ*, 686, 801
 Owocki S. P., Gayley K. G., 1997, in Nota A., Lamers H., eds, *Astronomical Society of the Pacific Conference Series* Vol. 120, *Luminous Blue Variables: Massive Stars in Transition*. p. 121
 Quinn T., Paczynski B., 1985, *ApJ*, 289, 634
 Ro S., Matzner C. D., 2016, *ApJ*, 821, 109
 Shankar F., Croce M., Miralda-Escudé J., Fosalba P., Weinberg D. H., 2010, *ApJ*, 718, 231
 Shapiro S. L., Teukolsky S. A., 1983, *Black holes, white dwarfs, and neutron stars: The physics of compact objects*
 Shaviv N. J., 2000, *ApJL*, 532, L137
 Shen Y., et al., 2007, *AJ*, 133, 2222
 Shu F. H., 1977, *ApJ*, 214, 488
 Sugimura K., Omukai K., Inoue A. K., 2014, *MNRAS*, 445, 544
 Susa H., 2013, *ApJ*, 773, 185
 Venemans B. P., et al., 2013, *ApJ*, 779, 24
 Volonteri M., 2010, *ARA&A*, 18, 279
 Volonteri M., Rees M. J., 2005, *ApJ*, 633, 624
 Wolcott-Green J., Haiman Z., Bryan G. L., 2011, *MNRAS*, 418, 838
 Wu X.-B., et al., 2015, *Nature*, 518, 512
 Żytkow A., 1972, *AcA*, 22, 103
 van Marle A. J., Owocki S. P., Shaviv N. J., 2009, *MNRAS*, 394, 595

This paper has been typeset from a $\text{\TeX}/\text{\LaTeX}$ file prepared by the author.